

On the interplay of electronic and lattice screening on exciton binding in two-dimensional lead halide perovskites

Rohit Rana^{1,2} and David T. Limmer^{1,2,3,4,*}

¹*Department of Chemistry, University of California, Berkeley, CA, USA, 94720*

²*Material Science Division Lawrence Berkeley National Laboratory, Berkeley, CA 94720, USA.*

³*Chemical Sciences Division, Lawrence Berkeley National Laboratory, Berkeley, CA 94720,*

⁴*Kavli Energy Nanoscience Institute, Berkeley, CA 94720*

(Dated: July 12, 2024)

We use path integral Monte Carlo to study the energetics of excitons in layered, hybrid organic-inorganic perovskites in order to elucidate the relative contributions of dielectric confinement and electron-phonon coupling. While the dielectric mismatch between polar perovskite layers and non-polar ligand layers significantly increases the exciton binding energy relative to their three-dimensional bulk crystal counterparts, formation of exciton polarons attenuates this effect. Dielectric confinement is well described by a fractional dimension scaling law as a function of layer thickness. The contribution from polaron formation is found to be a non-monotonic function of the lead halide layer thickness, which is clarified by a general variational theory. Accounting for both of these effects provides a description of exciton binding energies in good agreement with experimental measurements. By studying isolated layers and stacked layered crystals of various thicknesses, with ligands of varying polarity, we provide a systematic understanding of the excitonic behavior of this class of materials and how to engineer their photophysics.

A fundamental understanding of the photophysics of semiconducting materials is crucial for the engineering of efficient photovoltaic devices. One class of materials that has received significant recent attention are two-dimensional, layered lead halide perovskites due to their high operating efficiencies and robustness.¹⁻³ It is known that two-dimensional materials generally exhibit large, tunable exciton binding energies due to their strong Coulomb interactions resulting from dielectric confinement.⁴⁻⁶ Experiments and theory on bulk, three-dimensional perovskite lattices suggest that charge-phonon coupling and polaron formation underpin many of their observed electronic properties, including the low exciton binding energies.⁷⁻¹¹ The combination of these two effects has made understanding the excited state properties of layered perovskites difficult as there are few theoretical techniques capable of handling both non-perturbatively. We study the interplay between dielectric confinement and charge-phonon interactions in layered perovskites using an imaginary time influence functional approach applied to a generalized Fröhlich model Hamiltonian.^{12,13} Here, we find that the incorporation of a dynamic lattice leads to a reduction in exciton binding energies, in opposition to the large increase due to dielectric confinement. Additionally, we find a non-monotonic dependence on the polaron binding energy as a function of lead halide layer thickness, and attribute it to an interplay between in-plane screening and polaronic localization.

Three-dimensional lead halide perovskites have long charge carrier lifetimes and high power conversion efficiencies, but these semiconductors suffer from stability problems that limit their use.¹⁴⁻¹⁷ In contrast, two-dimensional layered lead halide perovskites, such

as Ruddlesden-Popper phases, have improved shelf-life and tunability due to the addition of barrier ligand layers.¹⁸⁻²⁰ As a consequence they are actively investigated for optoelectronic applications. However, due to the heterogeneous composition of these layered materials, their photophysics are different than their three-dimensional counterparts.^{18,21,22} Specifically, layered perovskites are quantum confined due to the small thickness of a typical inorganic layer relative to the excitonic radius.²³ The dielectric contrast between the organic and inorganic layers leads to an enhancement of the electrostatic interaction between the electron and hole of an exciton.^{21,23-25} Moreover, excitonic properties are renormalized due to charge-phonon interactions arising from the soft inorganic lattice, and the interplay of these interactions together with quantum and dielectric confinement remain to be understood in layered perovskites.^{22,24}

Computationally, the presence of exciton-phonon interactions leads to a breakdown of the Born-Oppenheimer approximation, making it challenging to accurately solve for the electronic structure for such systems. These considerations motivate the use of path integrals methods²⁶⁻²⁹ which can incorporate electron-hole interactions and charge lattice interactions at arbitrary strengths.^{11,30,31} In this work, we employ an imaginary time influence functional approach to the thermal path integral to study a continuum model of electron and hole quasiparticles interacting with the layered perovskite lattice.^{11,30,32} As depicted in Fig. 1, we apply this approach to two model systems with organic ligands, *n*-butylammonium (BTA) and phenylethylammonium (PEA), of varying polarity and having stoichiometry $(\text{BTA})_2(\text{MA})_{n-1}\text{Pb}_n\text{I}_{3n+1}$

and $(\text{PEA})_2(\text{MA})_{n-1}\text{Pb}_n\text{I}_{3n+1}$, where n is the number of inorganic sublayers. Modifying n changes the quantum well thickness and consequently, the degree of confinement.^{21,22,24,25}

The model Hamiltonian we consider is defined as

$$\hat{\mathcal{H}} = \hat{\mathcal{H}}_{\text{eh}} + \hat{\mathcal{H}}_{\text{ph}} + \hat{\mathcal{H}}_{\text{int}} \quad (1)$$

where $\hat{\mathcal{H}}_{\text{eh}}$ corresponds to the electronic degrees of freedom, $\hat{\mathcal{H}}_{\text{ph}}$ corresponds to the phonon degrees of freedom, and $\hat{\mathcal{H}}_{\text{int}}$ corresponds to the interaction between the phonon and electronic degrees of freedom. We employ an effective mass approximation and define the electronic Hamiltonian as

$$\hat{\mathcal{H}}_{\text{eh}} = \frac{\hat{\mathbf{p}}_e^2}{2m_e} + \frac{\hat{\mathbf{p}}_h^2}{2m_h} + \hat{V}(|\hat{\mathbf{r}}_e - \hat{\mathbf{r}}_h|) \quad (2)$$

where the subscript e and h indicates electron and hole, $\hat{\mathbf{p}}$ and $\hat{\mathbf{r}}$ are the in-plane momentum and position operators, and $m_e = m_h = 0.20$ ²⁴ are the effective quasiparticle masses in units of the bare electron mass. Here, we use continuum electrostatics and define $\hat{V}(|\hat{\mathbf{r}}_e - \hat{\mathbf{r}}_h|)$ to be the electron-hole interaction at the equilibrium lattice geometry.

Layered perovskites are dielectrically inhomogeneous, with planar interfaces in the stacking direction separating polarizable inorganic layers which host optical excitations, and less polar ligand layers which act as barriers. As a consequence, the effective interaction between electrons and holes is more complicated than its three-dimensional, homogeneous dielectric equivalent. In a cylindrical coordinate system, the electrostatic potential at position $\mathbf{s} = (\mathbf{r}, z)$ created by an electron in the inorganic well layer at position $\mathbf{s}' = (\mathbf{r}', z')$ satisfies Poisson's equation. Within the inorganic region hosting the point charge at $(\mathbf{r} = 0, z)$,

$$\nabla^2 V(\mathbf{r}', z', z) = -\frac{4\pi e}{\epsilon_i} \delta(\mathbf{r}) \delta(z' - z) \quad z, z' \leq nd \quad (3)$$

where e is the fundamental charge, ϵ_i is the inorganic well layer dielectric constant, and d the thickness of a single inorganic layer. Outside of the first inorganic layer, the electrostatic potential satisfies $\nabla^2 V(\mathbf{r}', z', z) = 0$, and the full solution must satisfy the dielectric discontinuity boundary conditions

$$\epsilon_i \nabla V(\mathbf{r}', knd + lD, z) = \epsilon_o \nabla V(\mathbf{r}', knd + lD, z) \quad (4)$$

where ϵ_o is an organic layer dielectric constant, D is the width of the organic layer, and k, l index the locations of the dielectric boundaries. Throughout this work, the length of one inorganic sublayer d is 6.39\AA .^{24,25,33} We consider two distinct experimentally relevant dielectric geometries, as depicted in Fig. 1. The first is a thin film of inorganic material surrounded by two semi-infinite surrounding organic layers, in which case $k = \{0, 1\}$ and

the lD term is ignored.³⁴ In this case, the semi-infinite organic regions model exfoliated perovskites dispersed in organic solvents.³⁵ This is equivalent to the Rytova-Keldysh theory.^{36,37} The second geometry is a crystal or infinitely-alternating slab geometry^{38,39} where a unit cell consists of an inorganic layer of length nd , and organic layer of length $D = 8.81\text{\AA}$, 9.92\AA for BTA and PEA, respectively.³⁸ In this case, $k, l = \{-\infty, \infty\}$. For each geometry, we use analytic representations of the solutions of Poisson's equations in a Fourier-Bessel basis and then numerically inverse Fourier transform them to evaluate the electrostatic energy in our Monte Carlo simulations (SI). Additionally, since the exciton binding energies of the model systems have been measured to be much bigger than the dominant longitudinal optical mode phonon energies,²¹ we use high-frequency dielectric constants to parameterize the potential energy functions for both geometries. Specifically, the inorganic layers have a dielectric constant of $\epsilon_i = 6.1$.⁴⁰ For the organic layers, we use $\epsilon_o = 2.1$ ⁴¹ and $\epsilon_o = 3.3$ ⁴² for the BTA and PEA ligands, respectively.

Using the solution to Poisson's equation for either geometry, we can write the electron-hole interaction in Eq. 2 as

$$V(r) = -e \int_{z_e} \int_{z_h} P(z_e) P(z_h) V(r, z_e, z_h) dz_h dz_e \quad (5)$$

where $r = |\mathbf{r}_e - \mathbf{r}_h|$ is the in-plane distance between the electron and hole, z_e is the z coordinate of the electron, z_h is the z coordinate of the hole, and $P(z_e)$ and $P(z_h)$ are the marginalized probability densities for the electron and hole in z . Without loss of generality, we average out the z -dependencies in Eq. 5 using particle-in-a-box ground state probability densities for $P(z_e)$ and $P(z_h)$ for a box size of length nd . We find that the exciton binding energy does not change by more than a few meV if uniform probability densities are used instead. This observation is consistent with previous work where it was found that the exciton binding energy remains insensitive to the specific shape of the z -component densities within the inorganic quantum well.²²

We are interested in low energy excitations and low temperatures, so to incorporate the lattice in our model Hamiltonian, we assume that it is described by harmonic modes

$$\hat{\mathcal{H}}_{\text{ph}} = \frac{1}{2} \sum_{\mathbf{k}} (\hat{\mathbf{p}}_{\mathbf{k}}^2 + \hat{\omega}_{\mathbf{k}}^2 \hat{\mathbf{q}}_{\mathbf{k}}^2) \quad (6)$$

where $\hat{\mathbf{p}}_{\mathbf{k}}$ and $\hat{\mathbf{q}}_{\mathbf{k}}$ are mass-weighted, in-plane momentum and position coordinates of a phonon described by a wavevector of \mathbf{k} . We consider only long-wavelength longitudinal optical modes, treated as dispersionless $\omega_{\mathbf{k}} \approx \omega_{\text{LO}}$, where ω_{LO} corresponds to the longitudinal optical mode frequency, with $\omega_{\text{LO}} = 18.84$ THz for the BTA perovskites⁸ and $\omega_{\text{LO}} = 21.27$ THz for the PEA

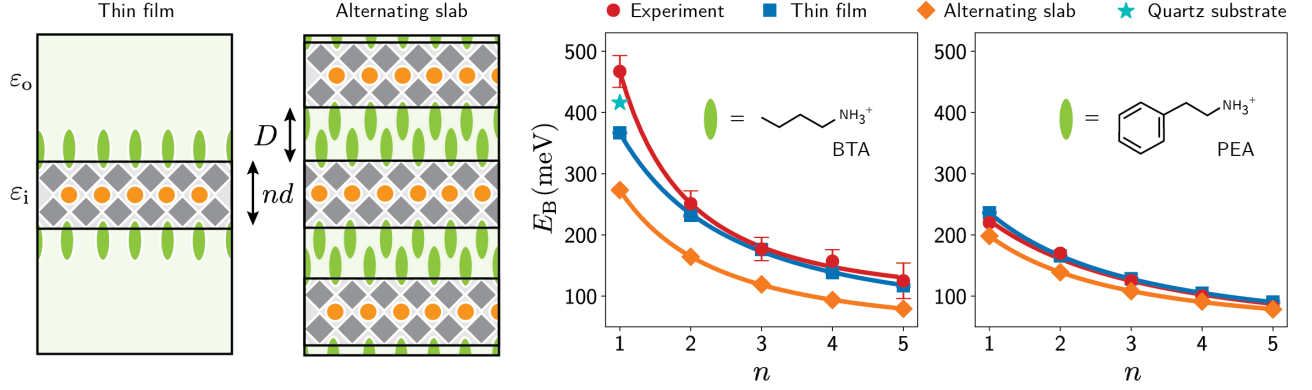


FIG. 1. Thin film geometry and renormalized exciton binding energies at different quantum well thicknesses for (left) BTA and (right) PEA perovskites. The inorganic well is modeled with a film of thickness nd and dielectric constant of ϵ_i . The organic ligands are modeled with semi-infinite thickness and a dielectric constant of ϵ_o . Circle markers represent experimental values obtained from literature. Square and diamond markers represent calculations done in this work for thin film and crystal geometries, respectively. Solid lines are fits to Eq. 17.

perovskites.⁹ We assume the charge-phonon interaction is bilinear, which allows us to write^{11,30,43}

$$\hat{\mathcal{H}}_{\text{int}} = \sqrt{\frac{2\omega_{\text{LO}}}{\hbar}} \sum_{\mathbf{k}} \hat{q}_{\mathbf{k}} \left[|g(\mathbf{k})| e^{i\mathbf{k}\cdot\hat{\mathbf{r}}_e} - |g(\mathbf{k})| e^{i\mathbf{k}\cdot\hat{\mathbf{r}}_h} \right] \quad (7)$$

where $|g(\mathbf{k})|$ represents the magnitude of the interaction strength and \hbar is the reduced Planck's constant. This form is sufficient to capture the interaction between each charge and the induced dipole of the lattice. The Hamiltonian in Eq. 7 could also be extended to higher temperatures using effective phonon theories.¹¹

The specific model for the charge-lattice coupling we consider is a generalized Fröhlich model derived for a charge screened by a longitudinal phonon in a thin film surrounded by two semi-infinite non-polarizable layers.^{13,44} This yields a charge-phonon interaction strength of

$$|g(\mathbf{k})| = \frac{\left[\frac{\pi e^2 nd \hbar \omega_{\text{LO}} (\epsilon_i^0 - \epsilon_i)}{2A} \right]^{1/2}}{\epsilon_o + nr_{\text{eff}} k} \quad (8a)$$

where

$$r_{\text{eff}} = \epsilon_o d \left[\frac{\epsilon_o}{3\epsilon_i} + \frac{\epsilon_i}{2\epsilon_o} \left(1 - \left[\frac{\epsilon_o^2}{\epsilon_i} \right]^2 \right) \right] \quad (8b)$$

is a dielectric screening length, A is the area of the unit cell, and $k = |\mathbf{k}|$. Throughout this work, we use a static dielectric constant of $\epsilon_i^0 = 13.0$.^{40,41} We note that when compared to three dimensional materials, the value of $(\epsilon_i^0 - \epsilon_i)$ is smaller for two dimensional materials due to the presence of fewer polarizable inorganic layers.⁴⁵

With all of the terms of the model Hamiltonian being appropriately defined, the partition function, \mathcal{Z} , can be expressed as a path integral

$$\mathcal{Z} = \int \mathcal{D}[\mathbf{r}_e, \mathbf{r}_h, \mathbf{q}_{\mathbf{k}}] \exp \left[-\frac{1}{\hbar} \mathcal{S}[\mathbf{r}_e, \mathbf{r}_h, \mathbf{q}_{\mathbf{k}}] \right] \quad (9)$$

where the Euclidean action \mathcal{S} is defined over an imaginary time τ as

$$\mathcal{S} = \int_0^{\beta\hbar} d\tau \mathcal{H}_{\text{eh},\tau} + \mathcal{H}_{\text{ph},\tau} + \mathcal{H}_{\text{int},\tau} \quad (10)$$

with $\beta = (k_{\text{B}}T)^{-1}$ where k_{B} is Boltzmann's constant, and T is the temperature of the system. Note that Eqs. 9 and 10 represent a classical isomorphism of the quantum Hamiltonian defined by Eq. 1. Since the phonon degrees of freedom are coupled linearly to the electronic degrees of freedom, the phonon degrees of freedom can be integrated out to yield

$$\mathcal{Z} = \mathcal{Z}_{\text{ph}} \int \mathcal{D}[\mathbf{r}_e, \mathbf{r}_h] \exp \left[-\frac{1}{\hbar} \mathcal{S}_{\text{eff}} \right] \quad (11)$$

where \mathcal{Z}_{ph} is the phonon partition function. The action corresponding to the effective Hamiltonian can be written as an imaginary time influence functional, (SI)

$$\mathcal{S}_{\text{eff}} = \int_{\tau} \frac{m_e}{2} \dot{\mathbf{r}}_e^2 + \frac{m_h}{2} \dot{\mathbf{r}}_h^2 + V(\mathbf{r}_e, \mathbf{r}_h) - \alpha \hbar \omega_{\text{LO}}^2 \sum_{i,j \in e,h} \Gamma_{i,j} \int_{\tau} \int_{\tau'} e^{-\omega_{\text{LO}}|\tau-\tau'|} f(|\mathbf{r}_{i,\tau} - \mathbf{r}_{j,\tau'}|) \quad (12)$$

where $\Gamma_{i,j} = 1$ for $i = j$ and -1 otherwise, while

$$\alpha = \frac{e^2 nd}{16n^2 r_{\text{eff}}^2 \hbar \omega_{\text{LO}}} (\epsilon_i^0 - \epsilon_i) \quad (13)$$

is a dimensionless coupling parameter and

$$f(r) = \int_{\mathbf{k}} \frac{e^{i\mathbf{k}\cdot\mathbf{r}}}{(\epsilon_o + nr_{\text{eff}}k)^2} \quad (14)$$

which can be analytically inverted in terms of Struve and Bessel functions.

For the path integral Monte Carlo method, we uniformly discretize the imaginary time interval in Eq. 11 into N slices. Then, we utilize the Metropolis-Hastings algorithm^{46,47} with proposed uniform displacements both of individual slices and the center of mass within a periodic two-dimensional box of 500×500 a.u. Additionally, we parameterize divergent attractive terms as $(r_c^2 + \mathbf{r}^2)^{1/2}$ rather than sole functions of \mathbf{r} . The parameter r_c is chosen such that the bandgap of the BTA and PEA perovskites are reproduced at $\mathbf{r} = 0$.^{11,30,48}

With path integral Monte Carlo, we can compute the exciton binding energy from

$$E_B = \lim_{T \rightarrow 0} \langle E_{eh} \rangle - \langle E_e \rangle - \langle E_h \rangle \quad (15)$$

where E_i is a simulation with ($i = eh$) an electron and hole, or ($i = e$) just an electron or ($i = h$) hole, and brackets denote thermal average. We use the virial estimator⁴⁹ to obtain values of the average energy at finite temperatures ranging from 50 K to 400 K. To extrapolate the ground-state exciton binding energy to 0 K, we use a two-level system fit in accordance with Boltzmann statistics that is parameterized with the ground-state exciton binding energy and the difference between the two energy levels. The large binding energies make this especially convenient. We used between 2 and 5 million Monte Carlo sweeps for each temperature to estimate averages.

We compute the exciton binding energy with the Hamiltonian defined in Eq. 1 as a function of increasing inorganic layer thickness, n . This yields insight into how quantum confinement, dielectric confinement, and electrostatic effects arising from the choice of geometry affect exciton binding energies. We find for the thinnest materials, the exciton binding energies are nearly an order of magnitude larger than their bulk three dimensional counterparts.¹¹ However, as shown in Fig. 1, we see that for larger values of n , there is a dramatic reduction in the exciton binding energy. These trends are a consequence of two factors. The first is that quantum confinement decreases for larger values of n , generally allowing charges to become more diffuse, weakening their interactions. The second is that dielectric confinement also decreases for larger values of n , so that the electron-hole interaction is more strongly screened by the more polarizable inorganic layer.

The role of quantum confinement can be assessed by considering the size of the exciton relative to the layer thickness. The size of the exciton is determined from its pair distribution function,

$$P(r) = \langle \delta(r - |\mathbf{r}_e - \mathbf{r}_h|) \rangle \quad (16)$$

in the low temperature limit. Figure 2 shows $P(r)$ computed for the exfoliated slab geometry. We find the exciton becomes more delocalized as n increases for both ligand systems. From $n = 1$ to $n = 5$ the exciton size, defined as the peak in $P(r)$, increases by nearly a factor of

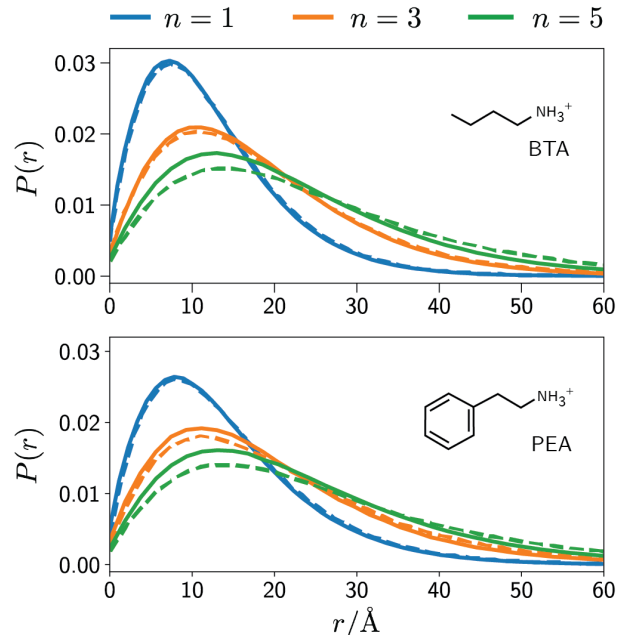


FIG. 2. Exciton probability densities of (top) BTA perovskites and (bottom) PEA perovskites as a function of quantum well thickness. Solid lines represent a bare exciton, and dashed lines account for exciton polaron formation.

2. This is a direct consequence of the reduced dielectric confinement for larger values of n . The size dependence is consistent with experimental observations that found a reduction of oscillator strength with increasing n as the size is correlated with the exciton overlap.³⁵ Although not presented in this work, we note that the same trends are obtained using the alternating slab model.

To understand the role of dielectric confinement, we compare the exciton binding energies for the two different ligand systems in Fig. 1 for a given geometry at a given value of n . We find the exciton binding energies of the PEA perovskites are smaller than the BTA perovskites. This is a result of the ligand dielectric environment becoming more similar to the inorganic perovskite layers, since the aromatic group on PEA is more polarizable. The reduced dielectric confinement in the PEA perovskites and their concomitant reduced binding energies also explains a previous observation showing that these materials have a higher photoluminescence quantum yield in comparison to the BTA perovskites.⁵⁰ For a given layered perovskite at a given value of n , Fig. 1 shows that the exciton binding energy is smaller for the alternating slab or crystal geometry than the film geometry. This is a result of a reduction in dielectric confinement due to an exciton in one inorganic layer being screened by other surrounding inorganic layers in the crystal geometry. This interaction is not present for the film geometry since it is assumed to be surrounded by organic solvent. Similar to the comparison of PEA per-

ovskites to BTA perovskites, we expect that crystalline layered perovskites have longer radiative lifetimes and higher photoluminescence quantum yields than their exfoliated counterparts.

Dielectric confinement can be modeled by an effective fractional-dimension scaling law^{21,25,51,52}

$$E_B = \frac{E_{3D}}{\left[1 - \frac{\Omega}{2}\right]^2} \quad (17)$$

where $\Omega = \kappa \exp[-nd/r_{3D}]$ is the difference in dimensionality from three, E_{3D} is the Rydberg energy, nd is the quantum well thickness, r_{3D} is the three-dimensional Bohr radius, and κ is a fitting parameter. For simplicity, we first use exciton binding energies obtained with simulations in the absence of phonons (Eq. 2) along with $E_{3D} = 37$ meV and $r_{3D} = 32$ Å.²⁵ For all of the layered perovskites studied in this work, we find Ω to be smaller than 2 for the $n = 1$ case. This exemplifies that quantum confinement in the z -direction is complemented with dielectric effects from the heterogeneous environment. Additionally, we find κ to take a range of 1.34 to 1.55. The perovskites with a larger value of κ will exhibit stronger dielectric confinement than those with smaller values of κ . This implies that two-dimensional systems with greater dielectric mismatch will require thicker layers to approach the bulk crystal regime than those with smaller mismatches. We further assess the utility of the scaling relation by parameterizing Eq. 17 with exciton binding energies obtained in the presence of a dynamic lattice (Eq. 1) and allowing E_{3D} , r_{3D} , and κ to all be fitting parameters. The resulting fits are shown as solid lines in Fig. 1 and model the data quite well. We also find the fitted bulk exciton binding energies and bulk exciton radii to be in good agreement with experiment.⁵³

The simulations shown in Fig. 1 also highlight that the minimal ingredients in our model are sufficient to predict theoretical exciton binding energies in good agreement with experiment. Specifically from Fig. 1, we see that the exciton binding energies obtained with the thin film geometry are in good agreement with experimental measurements of BTA exfoliated perovskites.²¹ Figure 1 shows that the renormalized exciton binding energies obtained with the crystal geometry of also shows good agreement with experimental values of PEA perovskite crystals.^{54,55} The only significant quantitative disagreement is the case of the $n = 1$ film geometry calculation in the BTA perovskite. However, we note that in the experimental setup, the exfoliated perovskites are placed on top of quartz substrates and are surrounded by vacuum for measurement of the binding energies. Therefore the simplifying assumption of being dispersed in a low dielectric solvent is not valid. A better model for this case is to employ a generalized film model where the layers surrounding the film on the top and bottom are different and the thin film is a composite dielectric.³⁴ To set

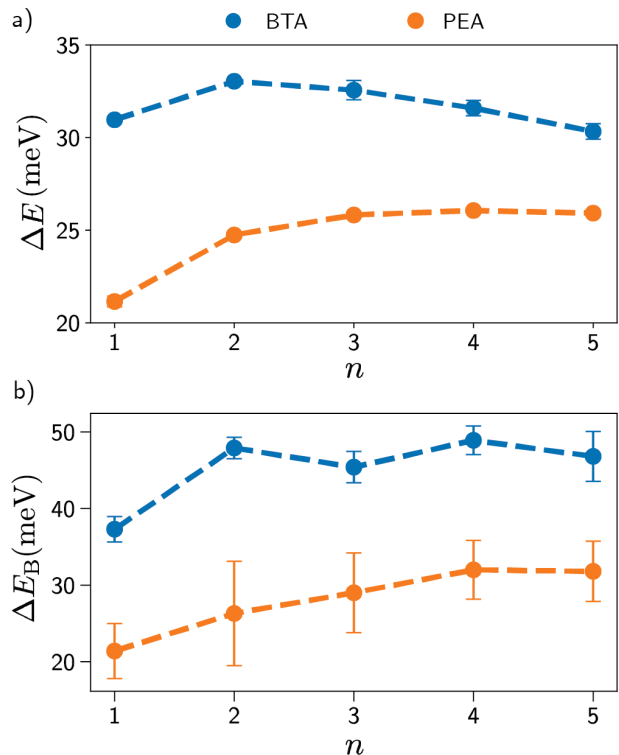


FIG. 3. a) Polaron binding energies and b) renormalization to exciton binding energies as a function of quantum well thickness for BTA and PEA perovskites.

up such a model we replace the inorganic layer with a thickness weighted dielectric constant^{35,38}

$$(\epsilon_i)_{\text{avg}} = \frac{\epsilon'_i nd + \epsilon'_o D}{nd + D} \quad (18)$$

for a film of length nd , where ϵ'_i and ϵ'_o are chosen to be 6.1 and 2.1, respectively. This thin film is placed in contact with a semi-infinite top surrounding layer of air with a dielectric constant of 1.0, and a semi-infinite bottom surrounding layer is chosen to be quartz with a dielectric constant of 3.9.⁵⁶ With this setup, we find the $n = 1$ renormalized exciton binding energy to be 416 meV, which is closer to the experimental value. For larger values of n , we find no significant differences in comparison to the exciton binding energies plotted in Fig. 1. This indicates that the role of the dielectric environment surrounding the inorganic perovskite layer becomes negligible for larger values of n .

The good quantitative agreement between theoretical exciton binding energies and experimental values is due in large part to the renormalization of the binding energy from polaron formation. This is demonstrated by computing the change in energy for a single electron (or hole) due to interactions with phonons. This quantity, also known as the polaron binding energy, is defined as

$$\Delta E = |\langle E_e \rangle_{\alpha \neq 0} - \langle E_e \rangle_{\alpha = 0}| \quad (19)$$

and extracted in the low temperature limit. From the data in Fig. 3 a), we find that the polaron binding energies are large in magnitude, thus highlighting that the soft lattice significantly stabilizes the free charges. Additionally, the polaron binding energy is larger in magnitude for the BTA perovskites in comparison to the PEA perovskites. Since the longitudinal optical mode frequencies and effective masses are similar in value for both perovskites, this larger polaron binding is a result of stronger dielectric confinement in the BTA system versus the PEA system. From Eq. 15 the exciton binding energy is the difference of the exciton energy and the free charges, so polaron formation reduces the exciton binding energy.

An offsetting factor to polaron formation is the stabilization of the exciton energy through exciton polaron formation. The renormalization to the exciton binding energy due to charge-phonon interactions are computed from

$$\Delta E_B = |(E_B)_{\alpha \neq 0} - (E_B)_{\alpha=0}| \quad (20)$$

in the low temperature limit and are shown in Fig. 3b). Our exciton polaron binding energies are also significant but smaller than twice the single charge polaron binding energies, the full stabilization of the free charges. We notice from Fig. 2 that for larger values of n where the renormalization to exciton binding is larger, the exciton becomes slightly more delocalized in comparison to the bare exciton. The n dependence can be understood by considering an exciton as a dipole. From Fig. 2, we observe that the increasing size of the exciton implies that the excitonic dipole moment increases as a function of n . For small values of n where the exciton has a smaller dipole moment, it will be harder for the exciton to interact with the polarization generated by the inorganic lattice.

Our calculations in Fig. 3a) show a non-monotonic change in polaron binding energy as function of n for both perovskites. In order to interpret this unanticipated dependence on layer thickness, we consider a weak coupling regime and derive a variational bound (SI). We use a free-particle trial action for an electron or hole, which we expect to be accurate since Fig. 2 shows that the excitonic pair distribution is moderately insensitive to the inclusion of exciton-phonon interactions. The free-particle trial action is defined as

$$\mathcal{S}_0 = \int_0^{\beta\hbar} d\tau \frac{m_e}{2} \dot{\mathbf{r}}_e^2. \quad (21)$$

and the Feynman-Bogolyubov inequality²⁶ implies

$$\Delta E \geq -E_0 - \frac{1}{\beta} \langle \mathcal{S}_e - \mathcal{S}_0 \rangle_0 \quad (22)$$

where E_0 is the energy associated with the trial action, \mathcal{S}_e is the action for an electron interacting with the lattice, and the expectation value is evaluated with respect to the

distribution associated with that trial action. Evaluation of Eq. 22 provides a bound

$$\Delta E \geq \alpha \hbar \omega_{LO} \xi \left(\frac{nr_{\text{eff}}}{\epsilon_0} \left/ \sqrt{\frac{\hbar}{2m_e \omega_{LO}}} \right. \right) \quad (23)$$

where the dimensionless scaling function, ξ ,

$$\xi(a) = 4 \frac{(a^4 - a^2) \ln(a) + \pi a^3 - a^2 - a^4}{(1 + a^2)^2} \quad (24)$$

depends on the ratio of the dielectric confinement length $nr_{\text{eff}}/\epsilon_0$ to the polaron radius $\sqrt{\hbar/2m_e \omega_{LO}}$. The non-monotonic behavior is captured by the bound, as α increases with layer thickness nd while ξ is a decreasing function of layer thickness. A maximum is predicted where the two lengths are equal, also consistent with our calculations. The bound, however, underestimates the binding energy, and it is not easily extendable to an equivalent bound for the exciton polaron energy.

Physically, the maximum in polaron binding results from two competing mechanisms. First, as n increases, there is more polarizable material present in the film layer. From this, we expect the electron-phonon interaction to increase⁴⁵ as a function of n . However, as n increases, it is easier to form a dipole in the lattice because it is better screened by the surrounding environment. As a consequence the effective dipole strength decreases, in turn also decreasing the reaction field from the charge and causing the stabilization of the polaron to lessen.

By accounting for dynamical screening arising from charge-phonon interactions, we find exciton binding energies of two model layered perovskites to be in good agreement with experiment. Specifically, we parameterize and evaluate a Fröhlich-like model Hamiltonian with a path integral Monte Carlo framework that allows us to capture higher levels of electron-hole correlations not easily obtained in conventional electronic structure methods like GW/BSE.⁵⁷ Additionally, a non-trivial trend in the polaron binding energy was uncovered and physically characterized through a variational bound. In summary, the complex interplay between quantum confinement, dielectric confinement, and charge-phonon interactions can be analyzed through the framework established in this work. Our approach suggests a promising avenue towards the design and understanding of photovoltaic devices.

The source code for the Monte Carlo calculations, and the code used to generate the figures are openly available online.⁵⁸

This work was supported by the US Department of Energy, Office of Science, Office of Basic Energy Sciences, Materials Sciences and Engineering Division, under Contract No. DE-AC02-05CH11231 within the Fundamentals of Semiconductor Nanowire Program (KCPY23). D.T.L. acknowledges the Alfred P. Sloan Foundation.

-
- * dlimmer@berkeley.edu.
- [1] Y.-T. Li, L. Han, H. Liu, K. Sun, D. Luo, X.-L. Guo, D.-L. Yu, and T.-L. Ren, Review on organic–inorganic two-dimensional perovskite-based optoelectronic devices, *ACS Applied Electronic Materials* **4**, 547 (2022).
 - [2] L. Mao, C. C. Stoumpos, and M. G. Kanatzidis, Two-dimensional hybrid halide perovskites: principles and promises, *Journal of the American Chemical Society* **141**, 1171 (2018).
 - [3] S. Ghimire and C. Klinker, Two-dimensional halide perovskites: synthesis, optoelectronic properties, stability, and applications, *Nanoscale* **13**, 12394 (2021).
 - [4] T. C. Berkelbach and D. R. Reichman, Optical and excitonic properties of atomically thin transition-metal dichalcogenides, *Annual Review of Condensed Matter Physics* **9**, 379 (2018).
 - [5] M. Velický and P. S. Toth, From two-dimensional materials to their heterostructures: An electrochemist’s perspective, *Applied Materials Today* **8**, 68 (2017).
 - [6] R. Chakraborty, G. Paul, and A. J. Pal, Quantum confinement and dielectric deconfinement in quasi-two-dimensional perovskites: Their roles in light-emitting diodes, *Physical Review Applied* **17**, 054045 (2022).
 - [7] Z. Gan, Y. Cheng, W. Chen, K. P. Loh, B. Jia, and X. Wen, Photophysics of 2d organic–inorganic hybrid lead halide perovskites: progress, debates, and challenges, *Advanced Science* **8**, 2001843 (2021).
 - [8] L. Ni, U. Huynh, A. Cheminal, T. H. Thomas, R. Shivanina, T. F. Hinrichsen, S. Ahmad, A. Sadhanala, and A. Rao, Real-time observation of exciton–phonon coupling dynamics in self-assembled hybrid perovskite quantum wells, *ACS nano* **11**, 10834 (2017).
 - [9] D. B. Straus, S. Hurtado Parra, N. Iotov, J. Gebhardt, A. M. Rappe, J. E. Subotnik, J. M. Kikkawa, and C. R. Kagan, Direct observation of electron–phonon coupling and slow vibrational relaxation in organic–inorganic hybrid perovskites, *Journal of the American Chemical Society* **138**, 13798 (2016).
 - [10] D. T. Limmer and N. S. Ginsberg, Photoinduced phase separation in the lead halides is a polaronic effect, *The Journal of chemical physics* **152** (2020).
 - [11] Y. Park, A. Obliger, and D. T. Limmer, Nonlocal screening dictates the radiative lifetimes of excitations in lead halide perovskites, *Nano Letters* **22**, 2398 (2022).
 - [12] H. Fröhlich, Electrons in lattice fields, *Advances in Physics* **3**, 325 (1954).
 - [13] W. H. Sio and F. Giustino, Unified ab initio description of Fröhlich electron–phonon interactions in two-dimensional and three-dimensional materials, *Physical Review B* **105**, 115414 (2022).
 - [14] D. Shi, V. Adinolfi, R. Comin, M. Yuan, E. Alarousu, A. Buin, Y. Chen, S. Hoogland, A. Rothenberger, K. Katsiev, *et al.*, Low trap-state density and long carrier diffusion in organolead trihalide perovskite single crystals, *Science* **347**, 519 (2015).
 - [15] K. Lin, J. Xing, L. N. Quan, F. P. G. de Arquer, X. Gong, J. Lu, L. Xie, W. Zhao, D. Zhang, C. Yan, *et al.*, Perovskite light-emitting diodes with external quantum efficiency exceeding 20 per cent, *Nature* **562**, 245 (2018).
 - [16] D. W. de Quilettes, S. M. Vorpahl, S. D. Stranks, H. Nagaioka, G. E. Eperon, M. E. Ziffer, H. J. Snaith, and D. S. Ginger, Impact of microstructure on local carrier lifetime in perovskite solar cells, *Science* **348**, 683 (2015).
 - [17] D. T. Gangadharan and D. Ma, Searching for stability at lower dimensions: current trends and future prospects of layered perovskite solar cells, *Energy & Environmental Science* **12**, 2860 (2019).
 - [18] P. Liu, S. Yu, and S. Xiao, Research progress on two-dimensional (2d) halide organic–inorganic hybrid perovskites, *Sustainable Energy & Fuels* **5**, 3950 (2021).
 - [19] T. L. Leung, I. Ahmad, A. A. Syed, A. M. C. Ng, J. Popović, and A. B. Djurišić, Stability of 2d and quasi-2d perovskite materials and devices, *Communications materials* **3**, 63 (2022).
 - [20] Y. Liu, M. Siron, D. Lu, J. Yang, R. Dos Reis, F. Cui, M. Gao, M. Lai, J. Lin, Q. Kong, *et al.*, Self-assembly of two-dimensional perovskite nanosheet building blocks into ordered Ruddlesden–Popper perovskite phase, *Journal of the American Chemical Society* **141**, 13028 (2019).
 - [21] J.-C. Blancon, A. V. Stier, H. Tsai, W. Nie, C. C. Stoumpos, B. Traore, L. Pedesseau, M. Kepenekian, F. Katsutani, G. Noe, *et al.*, Scaling law for excitons in 2d perovskite quantum wells, *Nature communications* **9**, 2254 (2018).
 - [22] K. R. Hansen, C. Y. Wong, C. E. McClure, B. Romrell, L. Flannery, D. Powell, K. Garden, A. Berzansky, M. Eggleston, D. J. King, *et al.*, Mechanistic origins of excitonic properties in 2d perovskites: Implications for exciton engineering, *Matter* **6**, 3463 (2023).
 - [23] E. Hanamura, N. Nagaosa, M. Kumagai, and T. Takagahara, Quantum wells with enhanced exciton effects and optical non-linearity, *Materials Science and Engineering: B* **1**, 255 (1988).
 - [24] Y. Cho and T. C. Berkelbach, Optical properties of layered hybrid organic–inorganic halide perovskites: A tight-binding GW-BSE study, *The Journal of physical chemistry letters* **10**, 6189 (2019).
 - [25] Y. Cho, S. M. Greene, and T. C. Berkelbach, Simulations of trions and biexcitons in layered hybrid organic–inorganic lead halide perovskites, *Physical Review Letters* **126**, 216402 (2021).
 - [26] R. P. Feynman, R. W. Hellwarth, C. K. Iddings, and P. M. Platzman, Mobility of slow electrons in a polar crystal, *Physical Review* **127**, 1004 (1962).
 - [27] D. Chandler and P. G. Wolynes, Exploiting the isomorphism between quantum theory and classical statistical mechanics of polyatomic fluids, *The Journal of Chemical Physics* **74**, 4078 (1981).
 - [28] D. M. Ceperley, Path integrals in the theory of condensed helium, *Reviews of Modern Physics* **67**, 279 (1995).
 - [29] J. Shumway and D. Ceperly, Quantum monte carlo methods in the study of nanostructures, *Encyclopedia of Nanoscience and Nanotechnology* (2004).
 - [30] Y. Park and D. T. Limmer, Renormalization of excitonic properties by polar phonons, *The Journal of chemical physics* **157** (2022).
 - [31] R. C. Remsing and J. E. Bates, Effective mass path integral simulations of quasiparticles in condensed phases, *The Journal of Chemical Physics* **153** (2020).
 - [32] Y. Park and D. T. Limmer, Biexcitons are bound in CsPbBr₃ perovskite nanocrystals, *Physical Review Materials* **7**, 106002 (2023).
 - [33] T. Oku, Crystal structures of CH₃NH₃PbI₃ and related perovskite compounds used for solar cells, *Solar Cells—New Approaches and Reviews* **1**, 77 (2015).

- [34] R. Barrera¹⁰, O. Guzman, and B. Balaguer, Point charge in a three-dielectric medium with planar interfaces, *Am. J. Phys* **46**, 11 (1978).
- [35] O. Yaffe, A. Chernikov, Z. M. Norman, Y. Zhong, A. Velauthapillai, A. Van Der Zande, J. S. Owen, and T. F. Heinz, Excitons in ultrathin organic-inorganic perovskite crystals, *Physical Review B* **92**, 045414 (2015).
- [36] N. S. Rytova, Screened potential of a point charge in a thin film, arXiv preprint arXiv:1806.00976 (2018).
- [37] L. Keldysh, Coulomb interaction in thin semiconductor and semimetal films, in *SELECTED PAPERS OF LEONID V KELDYSH* (World Scientific, 2024) pp. 155–158.
- [38] E. A. Muljarov, S. Tikhodeev, N. Gippius, and T. Ishihara, Excitons in self-organized semiconductor/insulator superlattices: Pbi-based perovskite compounds, *Physical Review B* **51**, 14370 (1995).
- [39] R. Guseinov, Coulomb interaction and excitons in a superlattice, *physica status solidi (b)* **125**, 237 (1984).
- [40] T. Ishihara, J. Takahashi, and T. Goto, Exciton state in two-dimensional perovskite semiconductor (c10h21nh3)2pbi4, *Solid state communications* **69**, 933 (1989).
- [41] T. Ishihara, J. Takahashi, and T. Goto, Optical properties due to electronic transitions in two-dimensional semiconductors (c n h 2 n+ 1 nh 3) 2 pbi 4, *Physical review B* **42**, 11099 (1990).
- [42] X. Hong, T. Ishihara, and A. Nurmikko, Dielectric confinement effect on excitons in pbi 4-based layered semiconductors, *Physical Review B* **45**, 6961 (1992).
- [43] R. P. Feynman, *Statistical mechanics: a set of lectures* (CRC press, 2018).
- [44] T. Sohler, M. Calandra, and F. Mauri, Two-dimensional fröhlich interaction in transition-metal dichalcogenide monolayers: Theoretical modeling and first-principles calculations, *Physical Review B* **94**, 085415 (2016).
- [45] W. H. Sio and F. Giustino, Polarons in two-dimensional atomic crystals, *Nature Physics* **19**, 629 (2023).
- [46] N. Metropolis, A. W. Rosenbluth, M. N. Rosenbluth, A. H. Teller, and E. Teller, Equation of state calculations by fast computing machines, *The journal of chemical physics* **21**, 1087 (1953).
- [47] W. K. Hastings, Monte carlo sampling methods using markov chains and their applications, "" (1970).
- [48] J. Schnitker and P. J. Rossky, An electron–water pseudopotential for condensed phase simulation, *The Journal of chemical physics* **86**, 3462 (1987).
- [49] M. Herman, E. Bruskin, and B. Berne, On path integral monte carlo simulations, *The Journal of Chemical Physics* **76**, 5150 (1982).
- [50] L. N. Quan, Y. Park, P. Guo, M. Gao, J. Jin, J. Huang, J. K. Copper, A. Schwartzberg, R. Schaller, D. T. Limmer, *et al.*, Vibrational relaxation dynamics in layered perovskite quantum wells, *Proceedings of the National Academy of Sciences* **118**, e2104425118 (2021).
- [51] X.-F. He, Excitons in anisotropic solids: The model of fractional-dimensional space, *Physical Review B* **43**, 2063 (1991).
- [52] H. Mathieu, P. Lefebvre, and P. Christol, Simple analytical method for calculating exciton binding energies in semiconductor quantum wells, *Physical Review B* **46**, 4092 (1992).
- [53] M. Baranowski and P. Plochocka, Excitons in metal-halide perovskites, *Advanced Energy Materials* **10**, 1903659 (2020).
- [54] G. Delport, G. Chehade, F. Lédée, H. Diab, C. Milesi-Brault, G. Trippé-Allard, J. Even, J.-S. Lauret, E. Deleporte, and D. Garrot, Exciton–exciton annihilation in two-dimensional halide perovskites at room temperature, *The journal of physical chemistry letters* **10**, 5153 (2019).
- [55] J. M. Urban, G. Chehade, M. Dyksik, M. Menahem, A. Surrente, G. Trippé-Allard, D. K. Maude, D. Garrot, O. Yaffe, E. Deleporte, *et al.*, Revealing excitonic phonon coupling in (pea)2(ma)n-1pbni3n+12d layered perovskites, *The Journal of Physical Chemistry Letters* **11**, 5830 (2020).
- [56] H. Zahra, A. Hichri, and S. Jaziri, Comparative study of the exciton binding energies of thin and ultrathin organic-inorganic perovskites due to dielectric mismatch effects, *Journal of Applied Physics* **122** (2017).
- [57] M. Röhlfing and S. G. Louie, Electron-hole excitations and optical spectra from first principles, *Physical Review B* **62**, 4927 (2000).
- [58] R. Rana, Code for "On the interplay of electronic and lattice screening on exciton binding in two-dimensional lead halide perovskites", 10.5281/zenodo.12683301 (2024).

Supplementary Material for “On the interplay of electronic and lattice screening on
exciton binding in two-dimensional lead halide perovskites”

Rohit Rana and David T. Limmer*

Department of Chemistry, University of California, Berkeley, CA, USA, 94720

(Dated: July 12, 2024)

arXiv:2407.08173v1 [cond-mat.mtrl-sci] 11 Jul 2024

*Electronic address: dlimmer@berkeley.edu.

I. DERIVATION OF EFFECTIVE ELECTRON-HOLE INTERACTION

A. Introduction

Our goal is to find the electron-phonon matrix element $|g(\mathbf{k})|$ for a Rytova-Keldysh film geometry. We will focus on longitudinal optical (LO) phonons. The polarization generated by an atomic displacement corresponding to a LO phonon with in-plane momentum \mathbf{k} is given as¹

$$\mathcal{P}(r, z) = \frac{e^2}{A} \sum_a \frac{Z_a \cdot (\mathbf{k}_{\text{LO}}^a / |\mathbf{k}_{\text{LO}}^a|)}{\sqrt{2M_a \omega_{\text{LO}} / \hbar}} p(z) e^{i\mathbf{k} \cdot \mathbf{r}} \quad (\text{S.1})$$

where the summation runs over the atoms of the unit cell. Here, Z_a is the Born effective charge tensor, A is the area of the unit cell, $p(z)$ is the z-direction polarization profile, e is the fundamental charge, \hbar is the reduced Planck's constant, ω_{LO} is the LO phonon frequency, and M_a is the mass of atom a . Without loss of generality, assume that the dielectric tensor is isotropic, and assume that the composition of the two layers surrounding the film layer are the same. Then, letting $k = |\mathbf{k}|$ we can write (see Appendix A of¹)

$$|g(\mathbf{k})| = \frac{C}{\varepsilon_i} \left[\frac{2}{knd} \left(1 + \frac{e^{-knd} - 1}{knd} \right) + \frac{2(1 - e^{-knd})^2 (\delta + \delta^2 e^{-knd})}{(knd)^2 (1 - \delta^2 e^{-2knd})} \right] \quad (\text{S.2a})$$

where

$$\delta = \frac{\varepsilon_i - \varepsilon_o}{\varepsilon_i + \varepsilon_o} \quad (\text{S.2b})$$

and

$$C = \frac{2\pi e^2}{A} \sum_a \frac{(\mathbf{k}/k) \cdot Z_a^m \cdot (\mathbf{k}_{\text{LO}}^a / |\mathbf{k}_{\text{LO}}^a|)}{\sqrt{2M_a \omega_{\text{LO}} / \hbar}} \quad (\text{S.2c})$$

Here, ε_i and ε_o denotes the inorganic layer high-frequency dielectric constant and the organic layer high-frequency dielectric constant, respectively. We use high-frequency dielectric constants here since the exciton binding energies are much greater than the dominant LO phonon energies for the systems in this work². Furthermore, the denominator of the full expression can be Taylor expanded to linear order in k to yield

$$|g(\mathbf{k})| \approx -i \frac{C}{\varepsilon_o + nr_{\text{eff}}k} \quad (\text{S.3a})$$

where

$$r_{\text{eff}} = \varepsilon_o d \left[\frac{\varepsilon_o}{3\varepsilon_i} + \frac{\varepsilon_i}{2\varepsilon_o} \left(1 - \left[\frac{\varepsilon_o}{\varepsilon_i} \right]^2 \right) \right] \quad (\text{S.3b})$$

For the majority of this work, since the dielectric constants of the layers differ considerably from each other, this approximate matrix element was found to be in good agreement with the full matrix element. Only in the case where the dielectric constants of layers become close to each other should it be necessary to use the full matrix element¹.

B. Getting rid of Born effective charges

A mass-weighted mode-effective Born effective charge tensor Z_v^* was used in Ref.³ to replace C in Eqs.S.2 and S.3 with

$$C' = \frac{2\pi e^2}{A} Z_v^* \sqrt{\frac{\hbar}{2M_o\omega_{LO}}} \quad (\text{S.4})$$

Here, M_o is an arbitrary reference mass used to keep the mode-effective Born charge tensor unit-less. Then, we can deal with the Born effective charge tensor by utilizing the following expression (Eqs. 5.79 and 5.84 in⁴)

$$\frac{(Z_v^*)^2}{\omega_{LO,v}} = \frac{\Omega M_o \omega_{LO,v}}{4\pi e^2} (\varepsilon^\infty)^2 \left(\frac{1}{\varepsilon^\infty} - \frac{1}{\varepsilon^0} \right) \quad (\text{S.5})$$

Here, $\Omega = A(nd + D)$ is the volume of a supercell consisting of one inorganic layer of length nd and one organic layer of length D . We can decompose the overall dielectric constant ε of the cell as

$$nd\varepsilon_i^{\infty,0} + D\varepsilon_o^{\infty,0} = (nd + D)\varepsilon^{\infty,0} \quad (\text{S.6})$$

Then, we obtain

$$\frac{(Z_v^*)^2}{\omega_{LO,v}} \approx \frac{AM_o\omega_{LO,v}}{4\pi e^2} [nd(\varepsilon_i^0 - \varepsilon_i^\infty)] \left(\frac{nd\varepsilon_i^\infty + D\varepsilon_o^\infty}{nd\varepsilon_i^0 + D\varepsilon_o^0} \right) \quad (\text{S.7})$$

Note that the organic layers in most layered perovskites are fairly non-polarizable. In such a case, the static and high-frequency dielectric constants of those layers are approximately the same. Also, we revert back to the notation of the main text where $\varepsilon_i = \varepsilon_i^\infty$. Then, in the limit of a Rytova-Keldysh geometry ($D \gg nd$), we have that

$$\frac{(Z_v^*)^2}{\omega_{LO,v}} \approx \frac{AM_o\omega_{LO,v}}{4\pi e^2} [nd(\varepsilon_i^0 - \varepsilon_i)] \quad (\text{S.8})$$

Plugging this back into the expression for $g(\mathbf{k})$ gives us

$$g(\mathbf{k}) = -i \frac{\left[\pi e^2 nd \hbar \omega_{LO} (\varepsilon_i^0 - \varepsilon_i) / 2A \right]^{1/2}}{\varepsilon_o + nr_{\text{eff}}k} \quad (\text{S.9})$$

Taking the magnitude of Eq. S.9 gives us Eq. 8a and 8b in the main text.

C. Electron and Hole Path Integral Formalism

Our aim is to derive an expression for $\hat{\mathcal{H}}_{\text{int},\tau}$ in Eq.10 of the main text. Following the derivation of Ref.⁵, the corresponding action \mathcal{S}_{int} to the charge-phonon interaction Hamiltonian can be written as

$$\mathcal{S}_{\text{int}} = -\frac{\omega_{LO}}{\hbar} \sum_{i,j} \int_{\tau} \int_{\tau'} \int_{\mathbf{k}} \Gamma_{ij} \chi_{\mathbf{k},\tau,\tau'} |g(\mathbf{k})|^2 e^{i\mathbf{k}\cdot[\mathbf{r}_{i,\tau} - \mathbf{r}_{j,\tau'}]} \quad (\text{S.10})$$

Here, $i, j \in \{e, h\}$ where e and h represent the electron and hole, respectively. Additionally, $\Gamma_{ij} = 1$ for $i = j$ and -1 otherwise, and χ represents the susceptibility function. We then use the bare susceptibility function at an imaginary time τ

$$\chi_{\mathbf{k},\tau} = \frac{e^{-\omega_{\text{LO}}|\tau|}}{2\omega_{\text{LO}}} \quad (\text{S.11})$$

This allows us to write the action as

$$\mathcal{S}_{\text{int}} = -\alpha \hbar \omega_{\text{LO}}^2 \sum_{i,j \in e,h} \Gamma_{ij} \int_{\tau} \int_{\tau'} e^{-\omega_{\text{LO}}|\tau-\tau'|} f(|\mathbf{r}_{i,\tau} - \mathbf{r}_{j,\tau'}|) \quad (\text{S.12a})$$

where

$$\alpha = \frac{e^2 n d}{16 n^2 r_{\text{eff}}^2 \hbar \omega_{\text{LO}}} (\varepsilon_i^0 - \varepsilon_i) \quad (\text{S.12b})$$

and $f(|\mathbf{r}_{i,\tau} - \mathbf{r}_{j,\tau'}|)$ is defined by

$$f(r) = \int_{\mathbf{k}} \frac{e^{i\mathbf{k}\cdot\mathbf{r}}}{(\varepsilon_o + n r_{\text{eff}} k)^2} \quad (\text{S.13})$$

We can further deal with the k space integral in Eq. S.13

$$\int_{\mathbf{k}} \frac{e^{i\mathbf{k}\cdot\mathbf{r}}}{(\varepsilon_o + n r_{\text{eff}} k)^2} = \left(\frac{A}{2\pi}\right) \left(\frac{1}{\varepsilon_o^2}\right) \int_0^\infty dk \frac{k J_0(kr)}{\left(1 + \frac{n r_{\text{eff}}}{\varepsilon_o} k\right)^2} \quad (\text{S.14})$$

Then, we obtain

$$f(r) = \left(\frac{A}{4\pi n^2 r_{\text{eff}}^2}\right) \left[\frac{2\varepsilon_o}{n r_{\text{eff}}} r + \pi \left(H_0\left(\frac{\varepsilon_o}{n r_{\text{eff}}} r\right) - Y_0\left(\frac{\varepsilon_o}{n r_{\text{eff}}} r\right) \right) - \frac{\pi \varepsilon_o}{n r_{\text{eff}}} r \left(H_1\left(\frac{\varepsilon_o}{n r_{\text{eff}}} r\right) - Y_1\left(\frac{\varepsilon_o}{n r_{\text{eff}}} r\right) \right) \right] \quad (\text{S.15})$$

II. ADDITIONAL SIMULATION DETAILS

In a path integral framework, our overall action after integrating out the phonon degrees of freedom is $\mathcal{S} = \mathcal{S}_{\text{eh}} + \mathcal{S}_{\text{int}}$. We first deal with \mathcal{S}_{eh} . After discretizing this action into N imaginary time slices, we have

$$\mathcal{S}_{\text{eh}} = \sum_{i=1}^N \frac{m_e N}{2\beta^2 \hbar^2} (\mathbf{r}_{e,i+1} - \mathbf{r}_{e,i})^2 + \sum_{i=1}^N \frac{m_h N}{2\beta^2 \hbar^2} (\mathbf{r}_{h,i+1} - \mathbf{r}_{h,i})^2 + \frac{1}{N} \sum_{i=1}^N V(r_i) \quad (\text{S.16})$$

where $\beta = (k_B T)^{-1}$ is the inverse temperature, m_e and m_h are the masses of the electron and hole, and $\mathbf{r}_{e,i}$ and $\mathbf{r}_{h,i}$ are the positions of the electron and hole at imaginary time i . Furthermore, the electrostatic potential V is defined by Eq.7 in the main text, and $r_i = |\mathbf{r}_{e,i} - \mathbf{r}_{h,i}|$. To deal with the divergence at $r_i = 0$, we make the electrostatic potential a function of $(r_c^2 + r^2)^{1/2}$ rather than sole functions of r . The parameter r_c is chosen such that the bandgap of the BTA and PEA perovskites are reproduced at $r = 0^{5-7}$. For simplicity, we use r_c values corresponding to the $n = 1$ bandgaps of the BTA⁸ and PEA⁹ perovskites for larger values of n . To validate the accuracy of this procedure, we find that numerical solutions for the Schrödinger equation for the Hamiltonian corresponding to \mathcal{S}_{eh} agree well with the corresponding path integral Monte Carlo results. The values of r_c used in this work are summarized in Table S1..

Lastly, in imaginary-time discretized form, the exciton-phonon action becomes

$$\mathcal{S}_{\text{int}} = -\frac{\alpha\beta\hbar^2\omega_{\text{LO}}^2}{N^2} \sum_{i,j \in e,h} \Gamma_{ij} \sum_{s \neq t} e^{-\frac{\beta\hbar\omega_{\text{LO}}}{N}|s-t|} f(|\mathbf{r}_{i,s} - \mathbf{r}_{j,t}|) \quad (\text{S.17})$$

where $s, t \in [1, N]$.

For the simulations, we find that $N = 200$ time slices provides sufficient convergence for the results obtained in this work. We run the simulations for between 2 and 5 million Monte Carlo sweeps and keep the acceptance rate to around 40% to ensure equilibration and sufficient statistics. For an efficient implementation of the kernel f defined by Eq. S.15 and S.17, we use highly accurate polynomial approximations of Struve and Bessel functions.¹⁰ It should also be noted that the solutions to Poisson's equation for both geometries in Eq. 5 of the main text can only be expressed analytically in momentum space¹¹⁻¹⁴. Then, we must numerically Fourier transform these solutions into position space in order to use them for simulation. We first describe the Fourier transform for the thin film geometry. For this case, the solution to Poisson's equation (Eq.3-5 of the main text) can be written as¹²

$$-eV(k, z_e, z_h) = -\frac{2\pi e^2}{\epsilon_i} \left(e^{-k|z_e - z_h|} + \frac{2\delta}{e^{2knd} - \delta^2} [\delta \cosh(k(z_e - z_h)) + e^{knd} \cosh(k(z_e + z_h - nd))] \right) \quad (\text{S.18})$$

where δ is defined in Eq. S.2 and $z_e, z_h \in [0, nd]$. We can now write a momentum space analogue to Eq.5 of the main text

$$V(k) = -e \int_{z_e} \int_{z_h} P(z_e) P(z_h) V(k, z_e, z_h) dz_h dz_e \quad (\text{S.19})$$

Then, we can use particle-in-a-box densities

$$P(z_i) = \frac{2}{nd} \sin^2\left(\frac{\pi z_i}{nd}\right) \quad (\text{S.20})$$

where $i \in \{e, h\}$, to write a quantum-confined thin film potential

$$V(k) = -\frac{2\pi e^2}{k\varepsilon_i[(knd)^2 + 4\pi^2]^2} \left[3(knd)^3 + 20\pi^2(knd) + \frac{32\pi^4}{(knd)^2} \left(\frac{1 - \delta(1 + knd) + e^{knd}(\delta + knd - 1)}{(e^{knd} - \delta)} \right) \right] \quad (\text{S.21})$$

Finally, we can Fourier transform $V(k)$ into r -space through the following integral

$$V(r) = \frac{1}{2\pi} \int_0^\infty kV(k)J_0(kr)dk \quad (\text{S.22})$$

The provided source code evaluates this integral for the thin film geometry through the Hankel transform library^{15,16}.

We use the same Fourier transform procedure for the alternating slab, crystal geometry. In this case, the solution to Poisson's equation in momentum space is written as¹¹

$$\begin{aligned} -eV(k, z_h, z_h) &= \frac{2\pi e^2}{\varepsilon_i k} \sinh(k|z_e - z_h|) - \frac{2\pi e^2}{\varepsilon_i k \sinh(k_o)} \left[2st \sinh(kD) \cosh(k(z_e + z_h + nd)) \right] \\ &\quad - \frac{2\pi e^2}{\varepsilon_i k \sinh(k_o)} \cosh(k(z_e - z_h)) \left[s^2 \sinh(k(nd + D)) + t^2 \sinh(k(D - nd)) \right] \end{aligned} \quad (\text{S.23a})$$

where

$$s = \frac{1}{2}(1 + \varepsilon_o/\varepsilon_i), \quad t = \frac{1}{2}(1 - \varepsilon_o/\varepsilon_i) \quad (\text{S.23b})$$

and

$$\frac{\varepsilon_o}{\varepsilon_i} \cosh(k_o) = s^2 \cosh(k(nd + D)) - t^2 \cosh(k(D - nd)) \quad (\text{S.23c})$$

When averaging out the z -dependencies from Eq. S.23, we use $P(z_i - nd)$ in Eq. S.20 to get a quantum-confined $V(k)$ similar to Eq. S.21. However, we highlight that trying to use this resulting $V(k)$ in Eq. S.22 is problematic due to the highly oscillatory nature of the integrand. This issue was resolved by Hansen et al.¹⁷ by setting the upper bound of the integral in Eq. S.22 as the value of k that maximizes the amplitude of the integrand for a given value of r . We then used the openly available code provided by these authors to conduct this procedure along with particle-in-a-box densities and the parameters listed in this work to get $V(r)$ for the crystal geometry.

III. DERIVATION OF VARIATIONAL BOUND

We start by considering a free electron trial action

$$\mathcal{S}_o = \int_0^{\beta\hbar} d\tau \frac{m_e}{2} \dot{\mathbf{r}}_e^2 \quad (\text{S.24})$$

where $\dot{\mathbf{r}}_e = \dot{\mathbf{r}}_e(\tau)$ represents the electron degrees of freedom at imaginary time τ . Then, the Feynmann-Bogolyubov inequality¹⁸ yields

$$\Delta E \geq -E_o - \frac{1}{\beta} \langle \mathcal{S}_e - \mathcal{S}_o \rangle_o \quad (\text{S.25})$$

where E_o is the energy associated with the trial action, \mathcal{S}_e is the action of a single electron interacting with the lattice through a thin-film Fröhlich interaction, and the expectation value is evaluated with respect to the distribution associated with the trial action. Then, the polaron binding energy is given in the low-temperature limit as

$$\Delta E \geq \lim_{k_B T \rightarrow 0} k_B T \left\langle \alpha \hbar \omega_{\text{LO}}^2 \int_0^{\beta\hbar} d\tau \int_0^{\beta\hbar} d\tau' e^{-\omega_{\text{LO}}|\tau-\tau'|} f(|\mathbf{r}_\tau - \mathbf{r}_{\tau'}|) \right\rangle_o \quad (\text{S.26})$$

We will first deal with the expectation value of f

$$\langle f(|\mathbf{r}_\tau - \mathbf{r}_{\tau'}|) \rangle_o = \frac{4\pi n^2 r_{\text{eff}}^2}{A} \sum_k \frac{1}{(\varepsilon_o + nr_{\text{eff}}k)^2} \langle e^{ik \cdot |\mathbf{r}_\tau - \mathbf{r}_{\tau'}|} \rangle_o = \frac{4\pi n^2 r_{\text{eff}}^2}{A\hbar} \sum_k \frac{1}{(\varepsilon_o + nr_{\text{eff}}k)^2} e^{-\hbar k^2 |\tau - \tau'| / (2m_e)} \quad (\text{S.27})$$

Our inequality now becomes

$$\begin{aligned} \Delta E &\geq \lim_{k_B T \rightarrow 0} k_B T \left[\frac{4\pi n^2 r_{\text{eff}}^2 \alpha \omega_{\text{LO}}^2}{A} \sum_k \frac{1}{(\varepsilon_o + nr_{\text{eff}}k)^2} \int_0^{\beta\hbar} d\tau \int_0^{\beta\hbar} d\tau' e^{-[\omega_{\text{LO}} + \hbar k^2 / (2m_e)]|\tau - \tau'|} \right] \\ &= \frac{4\pi n^2 r_{\text{eff}}^2 \alpha \omega_{\text{LO}}^2 m_h}{A} \sum_k \frac{1}{(\varepsilon_o + nr_{\text{eff}}k)^2} \cdot \frac{4\hbar}{\hbar k^2 + 2m_e \omega_{\text{LO}}} \end{aligned} \quad (\text{S.28})$$

Due to the spacing between successive \mathbf{k} , the sum can then be replaced by an integral

$$\frac{4\pi n^2 r_{\text{eff}}^2 \alpha \omega_{\text{LO}}^2 m_h}{A} \cdot \frac{A}{(2\pi)^2} \int_0^{2\pi} \int_0^{2\pi} dk d\phi \frac{4\hbar k}{(\hbar k^2 + 2m_e \omega_{\text{LO}})(\varepsilon_o + nr_{\text{eff}}k)^2} \quad (\text{S.29})$$

Evaluation of the integrand ultimately yields

$$\Delta E \geq \alpha \hbar \omega_{\text{LO}} \xi \left(\frac{nr_{\text{eff}}}{\varepsilon_o} \left/ \sqrt{\frac{\hbar}{2m_e \omega_{\text{LO}}}} \right. \right) \quad (\text{S.30})$$

where

$$\xi(a) = 4 \frac{(a^4 - a^2) \ln(a) + \pi a^3 - a^2 - a^4}{(1 + a^2)^2} \quad (\text{S.31})$$

depends on the ratio of the dielectric confinement length $nr_{\text{eff}}/\varepsilon_0$ to the polaron radius $\sqrt{\hbar/2m_e\omega_{\text{LO}}}$. ΔE is plotted as a function of n for the BTA and PEA perovskites in Fig.S1. Even though the quantitative agreement with Fig. 2a of the main text for small n can be improved upon with a better trial action, the bound derived in this work captures a non-monotonic behavior that qualitatively resembles the simulation results.

	BTA/Film	BTA/Crystal	PEA/Film	PEA/Crystal
r_c (au)	0.918	1.357	0.898	1.401
Band Gap (meV)	2.80	2.80	2.58	2.58

TABLE S1. Pseudopotential parameters r_c and bandgaps (Eq. S.16).

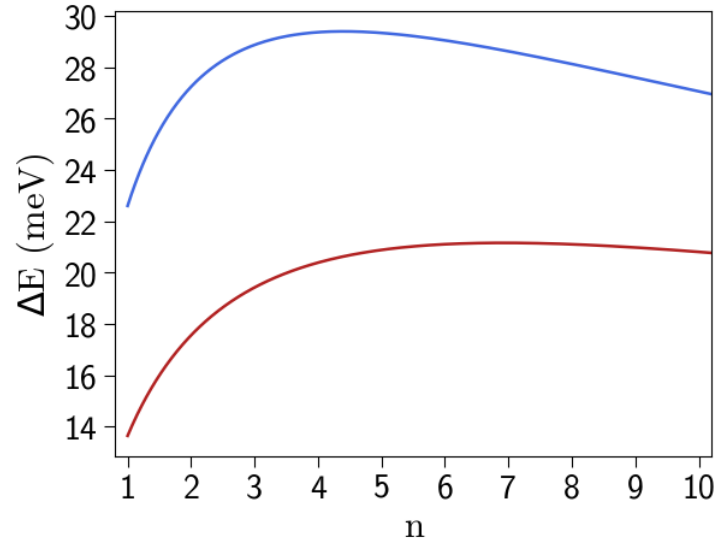


FIG. S1. Variational Bound (Eq. S.30 and S.31) as a function of inorganic well thickness. Top line and bottom line correspond to BTA and PEA perovskites, respectively.

-
- [1] T. Sohler, M. Calandra, and F. Mauri, *Physical Review B* **94**, 085415 (2016).
- [2] J.-C. Blancon, A. V. Stier, H. Tsai, W. Nie, C. C. Stoumpos, B. Traore, L. Pedesseau, M. Kepenekian, F. Katsutani, G. Noe, et al., *Nature communications* **9**, 2254 (2018).
- [3] W. H. Sio and F. Giustino, *Physical Review B* **105**, 115414 (2022).
- [4] O. Dolgov and E. Maksimov, *Modern Problems in Condensed Matter Sciences* **24**, 221 (1989).
- [5] Y. Park, A. Obliger, and D. T. Limmer, *Nano Letters* **22**, 2398 (2022).
- [6] J. Schnitker and P. J. Rossky, *The Journal of chemical physics* **86**, 3462 (1987).
- [7] Y. Park and D. T. Limmer, *The Journal of chemical physics* **157** (2022).
- [8] Y. Cho and T. C. Berkelbach, *The journal of physical chemistry letters* **10**, 6189 (2019).
- [9] D. B. Straus and C. R. Kagan, *Annual Review of Physical Chemistry* **73**, 403 (2022).
- [10] J. Newman, *Mathematics of Computation* **43**, 551 (1984).
- [11] E. A. Muljarov, S. Tikhodeev, N. Gippius, and T. Ishihara, *Physical Review B* **51**, 14370 (1995).
- [12] N. S. Rytova, arXiv preprint arXiv:1806.00976 (2018).
- [13] L. Keldysh, in *SELECTED PAPERS OF LEONID V KELDYSH* (World Scientific, 2024), pp. 155–158.
- [14] R. Barrera¹⁰, O. Guzman, and B. Balaguer, *Am. J. Phys* **46**, 11 (1978).
- [15] S. G. Murray and F. J. Poulin, arXiv preprint arXiv:1906.01088 (2019).
- [16] R. Rana, Code for “On the interplay of electronic and lattice screening on exciton binding in two-dimensional lead halide perovskites” (2024), URL <https://doi.org/10.5281/zenodo.12683301>.
- [17] K. R. Hansen, C. Y. Wong, C. E. McClure, B. Romrell, L. Flannery, D. Powell, K. Garden, A. Berzansky, M. Eggleston, D. J. King, et al., *Matter* **6**, 3463 (2023).
- [18] R. P. Feynman, R. W. Hellwarth, C. K. Iddings, and P. M. Platzman, *Physical Review* **127**, 1004 (1962).